Ablation Monitoring with a Regularized 3D Elastography Technique

Hassan Rivaz, Ioana Fleming, Mohammad Matinfar, Omar Ahmad,
Ali Khamene, Michael Choti, Gregory Hager and Emad Boctor

***Abstract*—We have previously developed regularized 2D and 3D elastography methods using Dynamic Programing (DP) [1], [2]. A cost function which incorporates similarity of echo amplitudes and displacement continuity was minimized using DP to obtain the displacement map. In this work, we present a novel hybrid method for calculating the displacement map between two ultrasound images. The method uses DP in the first step to find an initial estimate of the motion field. In the second step, we assume a linear interpolation for the reference image and obtain a closed-form solution for a subpixel accuracy motion field. The closed-form solution enables fast displacement estimation. We present three *in-vivo* patient studies of monitoring liver ablation with the hybrid elastography method. The thermal lesion was not discernable in the B-mode image but it was clearly visible in the strain image as well as in validation CT. We also present 3D strain images from thermal lesions in *ex-vivo* ablation. We introduce a novel volumetric rendering model for visualization of the volumetric B-mode images. We exploit strain values in the opacity of the volumetric B-mode data to better classify soft tissue. It is possible to observe the surface of the hard lesions, its size and its appearance from a single 3D rendering picture.**

I. Introduction

Ultrasound elastography has emerged as a useful augmentation to conventional ultrasound imaging [3]. Elastography has been used for monitoring RF ablation [4], [5] by observing that ablated region is harder than surrounding tissue. In the most common variation of elastography, ultrasound images are captured while the tissue is being compressed, and images are processed to provide a grid of local displacement measurements. These displacement fields are then used to determine the elastic properties of the tissue at each grid location. The grid of the elastic properties can be displayed as an image.

Elastography is computationally expensive, making it challenging to display strain images in real-time. Real-time feedback, however, is required for image guided ablation operations. Another aspect is that signal decorrelation between the pre- and post-compression images induces significant noise in the obtained displacement map and is one of the major limiting factors in elastography [6]. Methods based on cross-correlation and phase zero estimation are currently the most popular real-time elastography techniques which provide fast and accurate motion tracking. In RF ablation, however, high decorrelation between pre- and post-compression images results in high noise in the strain images obtained using cross-correlation [5]. Phase zero estimation methods require an estimate of the center frequency of the ultrasound RF signal, which varies with depth due to frequency-dependent attenuation in tissue [7]. This variation can be significant in RF ablation, leading to poor displacement estimation [7].

dynamic programming (DP) has been used recently for robust displacement estimation [8], [1], [2]. DP is more robust to signal decorrelation than standard cross-correlation methods and is therefore a good candidate for ablation monitoring where being real-time and robustness to noise are critically important. Here, we introduce a hybrid method that uses DP for an initial displacement estimation and refines the estimate by optimizing a regularized cost function. We use the method for processing 2D and 3D data for calculating 1D strain. We report *in-vivo* patient results on monitoring RF ablation with elastography and corroborate the results with CT scans. Finilly, we use a 3D probe to acquire 3D data and show that 3D elastography can be successfully used to monitor ablation in 3D using our novel visualization technique.

II. Hybrid Displacement Estimation

We provide an overview of the DP method first, followed by the description of the closed form solution for motion estimation. Compared to other optimization techniques, DP is an efficient non-iterative method of global optimization [9], [10]. In DP elastography, a cost function which incorporates similarity of echo amplitudes and displacement continuity is minimized. Since data alone can be insufficient to solve ambiguities of motion tracking due to signal decorrelation, the physical priors of tissue motion continuity increases the robustness of the technique [1]. We have showed that DP generates high quality strain images of freehand palpation elastography with up to 10% compression, indicating that the method is more robust to signal decorrelation (caused by scatterer motion in high axial compression and non-axial motions of the probe) in comparison to the standard correlation techniques. The 2D method operates in less than 1sec and is thus also suitable for real time elastography.

We now overview the formulation of 3D DP. Let $g_j^k(i)$ be the intensity of the i^{th} sample (axial direction), j^{th} A-line (lateral direction) and k^{th} frame (out-of-plane direction) of the pre-compression ultrasound volume. Let $g_{j+d_l}^{k+d_e}{}'(i+d_a)$ correspond to the post-compression volume where d_a, d_l and d_e represents axial, lateral and elevational displacements respectively, and the size of the volume be $m \times n \times p$. The difference between the two signals, Δ, can be quantified using

H. Rivaz, I. Fleming, M. Matinfar, O. Ahmad, G. Hager and E. Boctor are with ERC for Computer Integrated Surgery, Johns Hopkins University, Baltimore, MD. A. Khamene is with Siemens Corporate Research, Princeton, NJ. M. Choti is with Johns Hopkins Medical Institutes, Baltimore, MD.
Contact: rivaz@jhu.edu, eboctor1@jhmi.edu

sum of absolute differences (SAD), which is computationally inexpensive and is robust against outliers [11]:

$$\Delta(i,j,k,d_a,d_l,d_e) = \left| g_j^k(i) - g_{j+d_l}^{k+d_e\prime}(i+d_a) \right| \quad (1)$$

where the axial, lateral and elevational search ranges are limited by $d_{a,min} \leq d_a \leq d_{a,max}$, $d_{l,min} \leq d_l \leq d_{l,max}$ and $d_{e,min} \leq d_e \leq d_{e,max}$.

$$R(d_{a_i}, d_{l_i}, d_{e_i}, d_{a_{i-1}}, d_{l_{i-1}}, d_{e_{i-1}}) = (d_{a_i} - d_{a_{i-1}})^2 + (d_{l_i} - d_{l_{i-1}})^2 + (d_{e_i} - d_{e_{i-1}})^2 \quad (2)$$

is the smoothness regularization. The cost function at each point i, j and k is

$$C_j^k(d_a,d_l,d_e,i) = \Delta(i,j,k,d_a,d_l,d_e) + \min_{\delta_a,\delta_l,\delta_e} \left\{ \bar{C} \right\}, \quad (3)$$

$$\begin{aligned} \bar{C} &= \frac{C_j^k(\delta_a,\delta_l,\delta_e,i-1) + \left[C_{j-1}^k + C_j^{k-1}\right](\delta_a,\delta_l,\delta_e,i)}{3} \\ &+ wR(d_a,d_l,d_e,\delta_a,\delta_l,\delta_e) \end{aligned} \quad (4)$$

where w is a weight for enforcing smoothness. The inclusion of the costs of the previous point ($C_j^k(\delta_a,\delta_l,\delta_e,i-1)$), previous line ($C_{j-1}^k(\delta_a,\delta_l,\delta_e,i)$) and previous plane ($C_j^{k-1}(\delta_a,\delta_l,\delta_e,i)$) guarantees smoothness in the axial, lateral and elevational directions respectively. This form of $\bar{C}$ however requires the cost function of the all A-lines of the previous plane to be stored in the memory. We use an alternative form which requires storing only the cost function of the previous A-line on the processing plane:

$$\begin{aligned} & C_j^k(d_a,d_l,d_e,i) = \Delta(i,j,k,d_a,d_l,d_e) \\ &+ w_1 R(d_a,d_l,d_e,d_a^{k-1},d_l^{k-1},d_e^{k-1}) + \min_{\delta_a,\delta_l,\delta_e} \left\{ \bar{C} \right\}, \end{aligned} \quad (5)$$

$$\begin{aligned} \bar{C} &= \frac{C_j^k(\delta_a,\delta_l,\delta_e,i-1) + C_{j-1}^k(\delta_a,\delta_l,\delta_e,i)}{2} \\ &+ w_2 R(d_a,d_l,d_e,\delta_a,\delta_l,\delta_e) \end{aligned} \quad (6)$$

where w_1 is a weight for governing smoothness in the elevational direction and w_2 is a weight for governing axial and lateral smoothness. Equation 3 is preferred over Equation 5 since a wrong displacement estimation does not affect the neighboring A-line's displacement estimation. However we use the latter because of the memory limitations. Generally, the optimum values of $\delta_a, \delta_l, \delta_e$ should be sought in the entire $[d_{a,min}\ \ d_{a,max}] \times [d_{l,min}\ \ d_{l,max}] \times [d_{e,min}\ \ d_{e,max}]$ space. However, since the strain value is low in elastography, it is expected and desired that at each sample of RF data, the change between the displacement of a sample and its previous sample is not more than 1. Therefore, the search range is limited to the nine values of $\{d_a-1,\ d_a,\ d_a+1\} \times \{d_l-1,\ d_l,\ d_l+1\} \times \{d_e-1,\ d_e,\ d_e+1\}$, which results in a significant gain in speed. This limit on the search range does not affect the results even in a high strain of 10%: Δd is zero for nine samples and one for the tenth sample on average. We also limit the search range of each A-line to ± 1 of the previous A-line on the same plane. For memoization [9], δ_a, δ_l and δ_e values that minimize the cost function are stored:

$$M_j^k(i,d_i,d_l,d_e) = \arg \min_{\delta_a,\delta_l,\delta_e} \left\{ \bar{C} \right\} \quad (7)$$

The cost function C_j^k is calculated for $i = 1 \cdots m$, $d_a = d_{a,min} \cdots d_{a,max}$, $d_l = d_{l,min} \cdots d_{l,max}$ and $d_e = d_{e,min} \cdots d_{e,max}$. The minimum cost at $i = m$ gives the displacement of this point, which is traced back to $i = 1$ using the M function to calculate the three axial, lateral and elevational displacements ($D = (d_a, d_l, d_e)$):

$$\begin{aligned} D_j^k(i) &= \arg \min_{d_a,d_l,d_e} \left\{ C_j^k(d_a,d_l,d_e,i) \right\},\ i = m \\ D_j^k(i) &= M(i+1, D_j^k(i+1)),\quad i = 1 \cdots m-1 \end{aligned} \quad (8)$$

This gives all three displacements simultaneously, in contrast with other 3D elastography methods which give displacement in each direction in separate steps.

Further speed-up is achieved by downsampling the signal $g(i)$ in the axial direction by a factor of β to $g^*(i)$, and comparing it with the unaltered signal $g'(i)$. This is done by simply skipping $\beta - 1$ samples from $g(i)$ and performing DP on the β^{th} sample. This generates *integer displacement* estimations at m/β samples. The displacement of the skipped samples is then simply approximated by the linear interpolation of two neighboring points whose displacements are calculated, as an initial guess for the next step.

The displacement estimations from Equation 8 are used to estimate a subpixel displacement estimation by minimizing the following cost function:

$$\begin{aligned} C(f_1,\cdots,f_m) &= \Sigma_{i=1}^m \left[g_j^k(i) - g_{j+d_l}^{k+d_e\prime}(i + d_a(i) + f_i) \right]^2 \\ &+ w \left[d_a(i) + f_i - d_a(i-1) - f_{i-1} \right]^2 \end{aligned} \quad (9)$$

where f_i is the fractional displacement in the axial direction that is added to $d_a(i)$ at each sample i to obtain the final displacement field. w is again the regularization wieght. The cost function corresponds to the j^{th} A-line in the k^{th} plane. Assuming linear interpolation for $g_{j+d_l}^{k+d_e\prime}$, the above cost function becomes a parabolic function of f_i, $i = 1 \cdots m$, which has a closed form solution. Because of space limitations, more details of the algorithm cannot be presented here and will be published in a subsequent article.

III. 3D Visualization

Rendering 3D models from 3D ultrasonic data is a complicated task due to the noisy and fuzzy nature of ultrasound images. Ultrasound images contain considerable amount of noise, artifacts, and speckle. As reported in [12], ultrasound imaging posses features that cause well-known visualization techniques to fail. Among these features are significant amount of noise and speckle, lower dynamic range, and high variation in the intensity of neighboring voxels.

Our visualization algorithm is based on the standard volume rendering pipeline. We introduced a new element to this algorithm by using strain values in the opacity function to better classify soft tissues: The new opacity function is inferred from both B-mode and strain values. The current volume rendering algorithm is implemented using GPU.

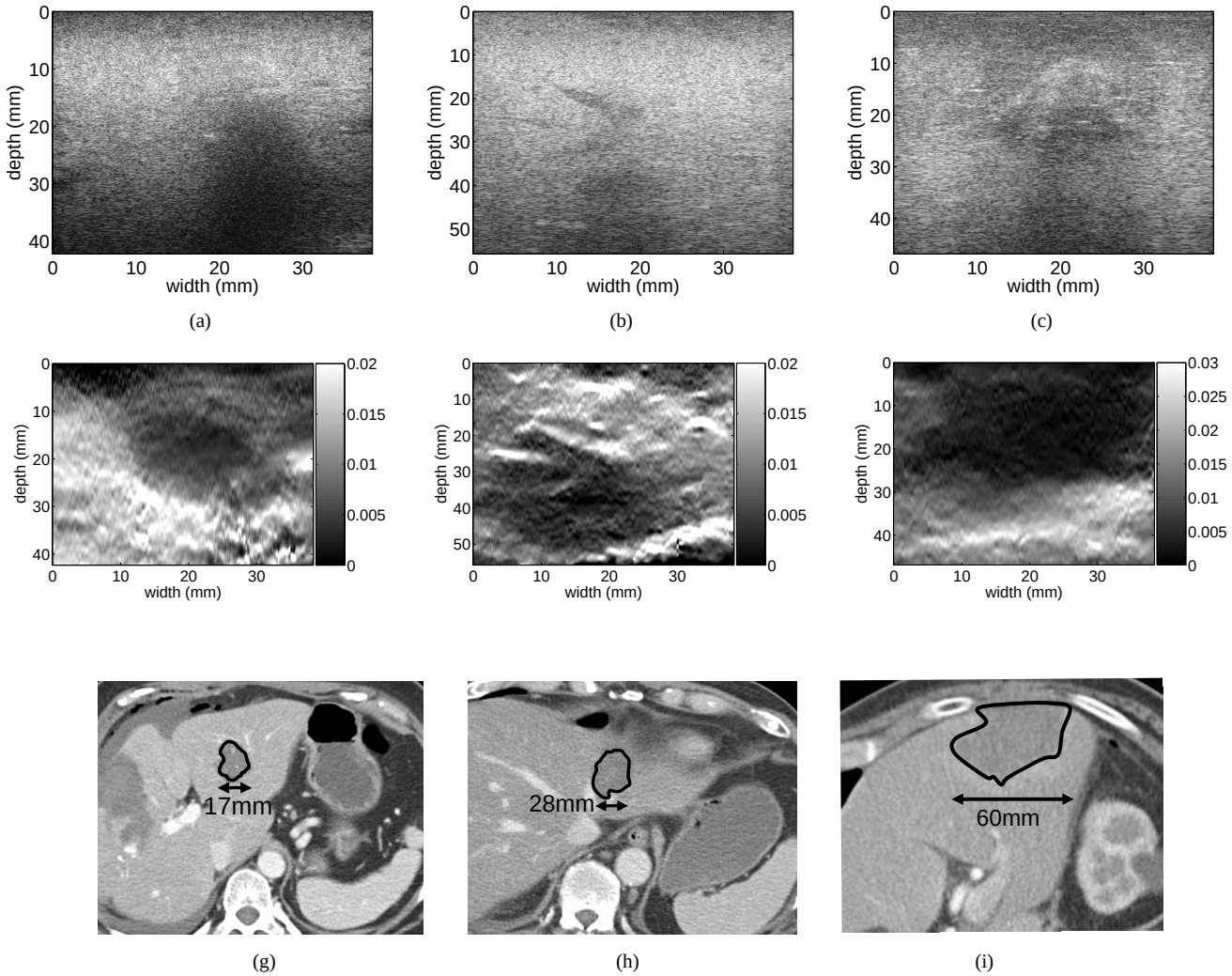

Fig. 1. *In-vivo* images of the thermal lesion produced by RF ablation therapy of liver cancer. First, second and third column correspond to the first, second and third patients. (a) - (c) B-scan after RF ablation. The shadow in (a) and (c) indicates the presence of thermal lesion. It is almost impossible to ascertain the size and position of the thermal lesion from the B-scans. (d) - (f) Strain images after RFA ablation, generated using 2D DP elastography and freehand palpation of the liver tissue. The thermal lesion is visible in dark surrounded by normal tissue in white. (g) - (i) Post-ablation CT scans, with the delineated thermal lesions (The non-unity aspect ratio in the axes of the B-mode and strain images should be considered when comparing them with the CT scans).

IV. Results

We first present *in-vivo* elastographic monitoring of RF ablation therapy of liver cancer in human during surgery using the novel elastography method. RF ablation was administered using the RITA Model 1500X RF generator (Rita Medical Systems, Fremont, CA). Ultrasound RF data is acquired from an Antares Siemens system (Issaquah, WA) with a 7.27MHz linear array at a sampling rate of 40MHz. The strain images are generated offline. We have an active IRB protocol for patient studies and we have monitored ablation in 5 patients to date. However, we show the results from only 3 patients due to space limitations. Figure 1 shows the B-mode scan, the strain image obtained using our elastography method and CT scans performed after RF ablation (first, second and third columns corresponding to first, second and third patients respectively). Tissue is simply compressed freehand with the ultrasound probe without any attachment. The shadow in Figure 1(a) at 20mm depth is produced by the thermal lesion. Note that it is not possible to ascertain the size and position of the thermal lesions from B-mode images. In addition, the thermal lesion has different appearances in the three B-scans. However, the thermal lesions show very well as hard lesions in the strain images. The size of the thermal lesion in the strain images and in CT scans are also in accordance. It seems that the strain images provide with higher contrast of the thermal lesion and lower noise in the image, compared to the strain images of RF ablation obtained with cross-correlation methods. However, a more rigorous validation of the size and shape of the ablated lesion in the regularized elastography method is necessary. To the best of our knowledge, this is also the first demonstration of the success of elastography in imaging the thermal lesion in an *in-vivo* human experiment.

For 3D elastography, we use a 3D probe that consists of a curvilinear array that is mechanically rotated to scan a volume. Ultrasound RF data is acquired from an Ultrasonix system (Vancouver, BC) at 4.5MHz frequency, 20MHz sampling rate

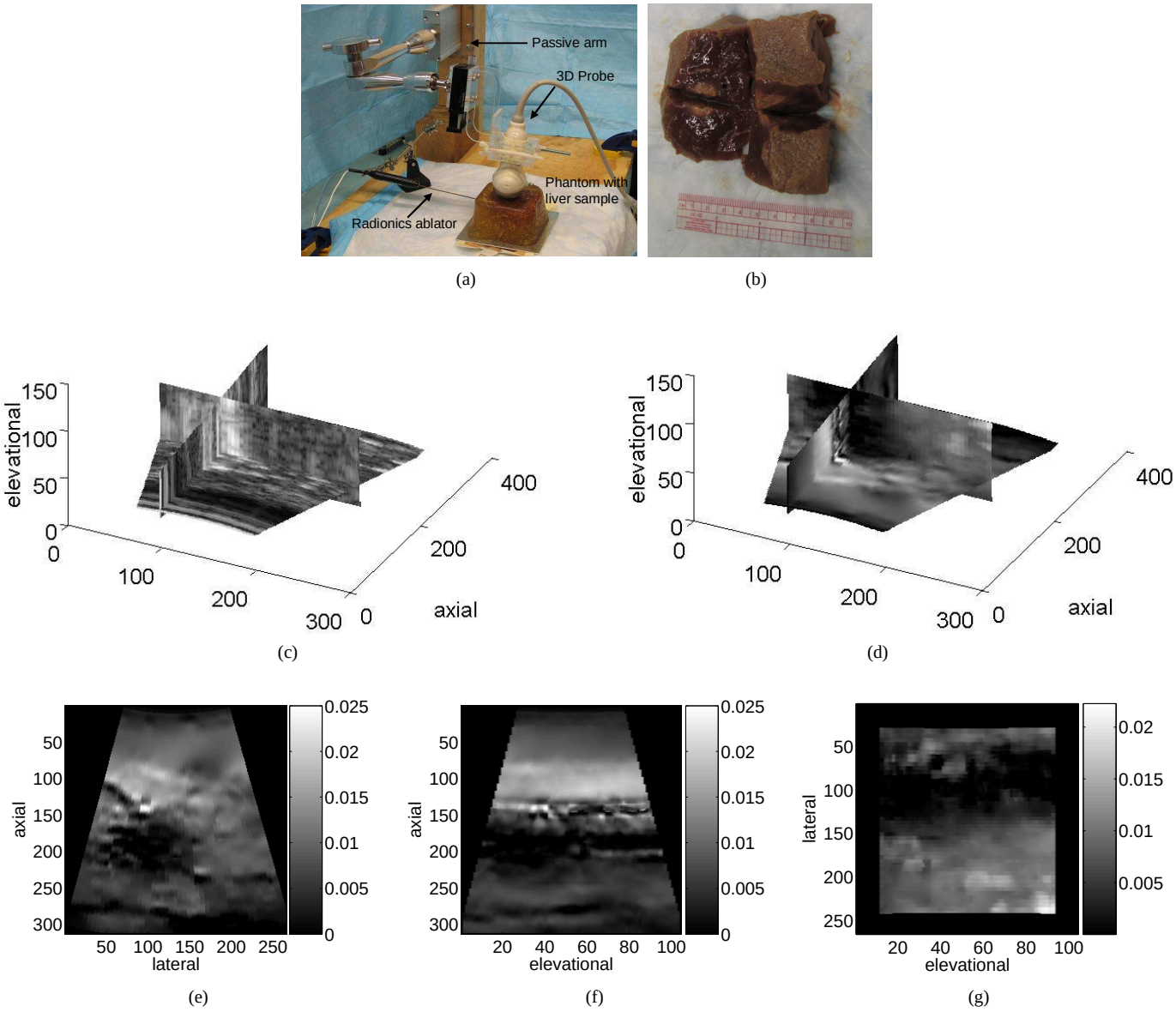

Fig. 2. *Ex-vivo* liver RF ablation experiment. (a) The experimental setup. The passive arm is holding the 3D probe and the liver is contained in the phantom. (b) The liver sample after ablation, cut into four pieces. (c) & (d) 3D B-mode and strain images after ablation. (e) - (g) 2D projections of the 3D strain image.

and 30% bandwidth. A Radionics device (Valleylab, Boulder, CO) is used for *ex-vivo* RF ablation. The ablation power is set to 8W for 10min and the cooler is turned off throughout the experiment. Target temperature reached 90°C in 3min and was kept constant in the next 7min of ablation. Figure 2 shows the experimental setup and results. There is a good agreement between the size of the lesion in the axial and lateral directions in the strain images and gross pathology. The ablation goes beyond the probe's field of view in the elevational direction. Figure 3 shows the volume rendering of the ultrasound image after ablation, clearly showing the ablated lesion.

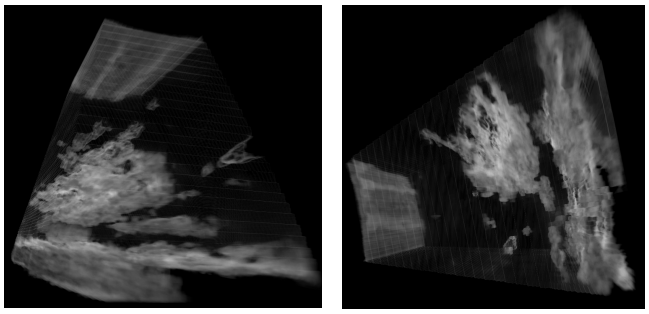

Fig. 3. *Ex-vivo* liver RF ablation experiment. Volume renderings of the 3D B-mode image using 3D strain in the opacity function.

V. Discussion and Conclusion

Strain images in Figure 1 demonstrate that the proposed regularized elastography method can be used to visualize the ablated region immediately after RF ablation. Elastography is challenging during ablation because of the dynamic changes in the image during thermal power deposition. We are cur-

rently working on implementing our method on the ultrasound machine to enable real-time monitoring of the ablation. To examine the feasibility of such monitoring, we have collected real-time strain images using Siemens Antares EI (Elastisity Imaging) module in one of the patient studies. Figure 4 (a) shows three small ablated lesions around ablator tines, which are grown over time to a large hard lesion in Figure 4 (c).

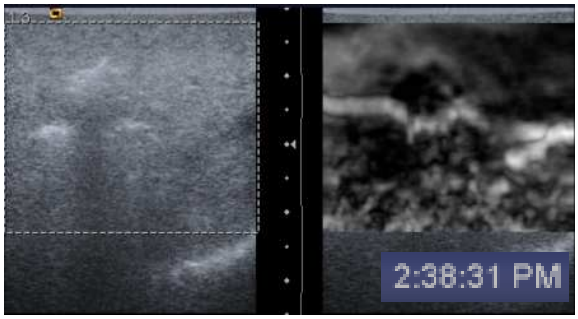

(a)

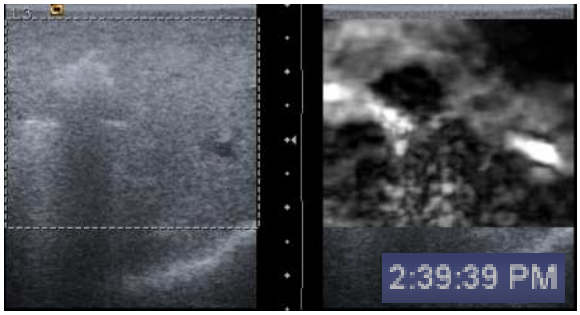

(b)

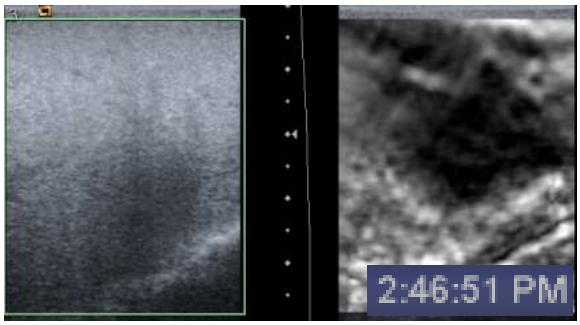

(c)

Fig. 4. RF ablation monitoring in a *in-vivo* patient study. B-mode and strain images are shown in the left and right respectively. The three images in (a) to (c) are acquired at three stages of the ablation (times shown on each image).

In this paper, we present high quality *in-vivo* 2D strain images of thermal lesions and compared them to post-ablation CT data. Comparison is more qualitative, however, since strain images are 2D and CT data is 3D and ultrasound is not tracked.

We also present formulation and experimental results of novel regularized elastography technique. An extensive study of the robustness and accuracy of the new regularized elastography technique is the subject of future research. We have shown before that regularization in DP increase robustness [1].

We demonstrate the feasibility of 3D elastography monitoring of RF ablation for the first time using a 3D probe; however, we are planning for a comprehensive comparison of the 3D elastography method with other 3D strain imaging techniques [13], [14] and with 3D temperature imaging implementations [15]. The lateral and elevational search is performed only to increase the quality of the axial strain: the lateral and elevational displacements are integer values and are not suitable for calculating strain.

Good volumetric CNR between the thermal lesion and background suggests that the regularization is not adversely affecting CNR. However, a study similar to [1] on the effect of the 3D regularization on the CNR and resolution should be done. Having an elastography system for 3D ablation monitoring with promising *ex-vivo* results, *in-vivo* patient studies under our active Institutional Review Board (IRB) approval are to commence.

Acknowledgment

Hassan Rivaz is supported by Link Foundation Fellowship and by Breast Cancer Predoctoral Traineeship Award from the Department of Defence. The authors would like to thank Siemens Medical Solutions and Ultrasonix Company for technical support and Dr. Sanjay Munireddy and Dr. Lia Assumpcao from Johns Hopkins Medicine for help with CT to ultrasound registration and data collection.

References

[1] H. Rivaz, E. Boctor, P. Foroughi, R. Zellars, G. Fichtinger, and G. Hager, "Ultrasound elastography: a dynamic programmimg approach," *IEEE Trans. Medical Imaging*, vol. 27, pp. 1373–1377, October 2008.

[2] H. Rivaz, I. Fleming, L. Assumpaco, G. Fichtinger, I. Choti, G. Hager, and E. Boctor, "Ablation monitoring with elastography: 2d in-vivo and 3d ex-vivo studies," *Medical Image Computing and Computer Assisted Intervention, MICCAI*, pp. 458–466, September 2008.

[3] J. Ophir, S. Alam, B. Garra, F. Kallel, E. Konofagou, T. Krouskop, and T. Varghese, "Elastography: ultrasonic estimation and imaging of the elastic properties of tissues," *Annu. Rev. Biomed. Eng.*, vol. 213, pp. 203–233, November 1999.

[4] R. Righetti, F. Kallel, R. Stafford, R. Price, T. Krouskop, Hazle, and J. Ophir, "Elastographic characterization of hifu-induced lesions in canine livers," *Ultrasound Med Biol*, vol. 25, no. 7, pp. 1099–1113, 1999.

[5] T. Varghese, J. Zagzebski, and F. Lee, "Elastographic imaging of thermal lesions in the liver in vivo following radiofrequency ablation: preliminary results," *Ultrasound Med. Biol.*, vol. 28, pp. 1467–1473, 2002.

[6] T. Varghese, J. Ophir, E. Konofagou, F. Kallel, and Righetti, "Tradeoffs in elastographic imaging," *Ultrason. Imag.*, vol. 23, pp. 216–248, 2001.

[7] H. Xie, T. Gauthier, and A. Fernandez, "The role of local center frequency estimation in doppler-based strain imaging," in *IEEE Ultrasonics Symp.*, (New York, NY), pp. 1965–1968, October 2007.

[8] J. Jiang and T. Hall, "A regularized real-time motion tracking algorithm using dynamic programming for ultrasonic strain imaging," in *IEEE Ultrasonics Symp.*, (Vancouver, Canada), pp. 606–609, October 2006.

[9] R. Bellman, *Applied dynamic programming*. Princeton U. Press, 1962.

[10] M. Brown, D. Burschka, and G. Hager, "Advances in computational stereo," *IEEE Trans. Pattern Analysis Machine Intelligence*, vol. 25, no. 8, pp. 993–1008, 2003.

[11] P. Huber, *Robust statistics*. John Wiley & Sons, 1981.

[12] G. Sakas and S. Walter, "Extracting surfaces from 3D-ultrasound data," *22nd Annual Conf. on Computer Graphics and Interactive Techniques*, pp. 465–474, April 1995.

[13] G. Treece, J. Lindop, A. Gee, and R. Prager, "Freehand elastography using a 3-D probe," *Ultrasound Med. Biol.*, vol. in press.

[14] T. Fisher, J. Jiang, and T. Hall, "Volumetric strain imaging," in *IEEE Ultrasonics Symp.*, (New York, NY), pp. 355–358, October 2007.

[15] A. Anand, D. Savery, and C. Hall, "Thee-dimentional spatial and temporal temprature imaging in gel phantoms using backscattered ultrasound," *IEEE Trans Ultrason Ferroelectr Freq Control*, vol. 54, pp. 23–31, 2007.